


Article

Bimetallic Pt-Ni Nanoparticles Confined in Porous Titanium Oxide Cage for Hydrogen Generation from NaBH₄ Hydrolysis

Yuqian Yu ^{1,†}, Li Kang ^{1,†}, Lixian Sun ^{1,2,*} , Fen Xu ^{1,*}, Hongge Pan ^{3,*}, Zhen Sang ¹, Chenchen Zhang ¹, Xinlei Jia ¹, Qingli Sui ¹, Yiting Bu ¹, Dan Cai ¹, Yongpeng Xia ¹, Kexiang Zhang ¹ and Bin Li ¹

- ¹ Guangxi Key Laboratory of Information Materials, Guangxi Collaborative Innovation Center for Structure and Properties for New Energy and Materials, School of Material Science and Engineering, Guilin University of Electronic Technology, Guilin 541004, China; yuyuqian997@163.com (Y.Y.); kangli000hello@163.com (L.K.); 15755028821@163.com (Z.S.); Zhang_linba_3760@163.com (C.Z.); jia15292079581@163.com (X.J.); sqlguet123@163.com (Q.S.); ytb1172701255@163.com (Y.B.); dancai1985@guet.edu.cn (D.C.); ypxia@guet.edu.cn (Y.X.); kxzhang@guet.edu.cn (K.Z.); li_bin@guet.edu.cn (B.L.)
- ² School of Mechanical & Electrical Engineering, Guilin University of Electronic Technology, Guilin 541004, China
- ³ School of New Energy Science and Technology, Xi'an Technological University, Xi'an 710021, China
- * Correspondence: sunlx@guet.edu.cn (L.S.); xufen@guet.edu.cn (F.X.); hgpan@zju.edu.cn (H.P.)
- † These authors contributed equally to this work.

Abstract: Sodium borohydride (NaBH₄), with a high theoretical hydrogen content (10.8 wt%) and safe characteristics, has been widely employed to produce hydrogen based on hydrolysis reactions. In this work, a porous titanium oxide cage (PTOC) has been synthesized by a one-step hydrothermal method using NH₂-MIL-125 as the template and L-alanine as the coordination agent. Due to the evenly distributed PtNi alloy particles with more catalytically active sites, and the synergistic effect between the PTOC and PtNi alloy particles, the PtNi/PTOC catalyst presents a high hydrogen generation rate (10,164.3 mL·min⁻¹·g⁻¹) and low activation energy (28.7 kJ·mol⁻¹). Furthermore, the robust porous structure of PTOC effectively suppresses the agglomeration issue; thus, the PtNi/PTOC catalyst retains 87.8% of the initial catalytic activity after eight cycles. These results indicate that the PtNi/PTOC catalyst has broad applications for the hydrolysis of borohydride.

Keywords: hydrogen generation; porous titanium oxide cage; PtNi nanoparticles; sodium borohydride hydrolysis



Citation: Yu, Y.; Kang, L.; Sun, L.; Xu, F.; Pan, H.; Sang, Z.; Zhang, C.; Jia, X.; Sui, Q.; Bu, Y.; et al. Bimetallic Pt-Ni Nanoparticles Confined in Porous Titanium Oxide Cage for Hydrogen Generation from NaBH₄ Hydrolysis. *Nanomaterials* **2022**, *12*, 2550. <https://doi.org/10.3390/nano12152550>

Academic Editor: Yuichi Negishi

Received: 29 June 2022

Accepted: 21 July 2022

Published: 25 July 2022

Publisher's Note: MDPI stays neutral with regard to jurisdictional claims in published maps and institutional affiliations.



Copyright: © 2022 by the authors. Licensee MDPI, Basel, Switzerland. This article is an open access article distributed under the terms and conditions of the Creative Commons Attribution (CC BY) license (<https://creativecommons.org/licenses/by/4.0/>).

1. Introduction

The overconsumption of traditional fossil fuels has brought in severe energy shortages and environmental pollution issues, such as the greenhouse effect [1]. To solve the above issues, hydrogen energy, as an efficient and sustainable energy, is considered to be a promising alternative to fossil energy [2,3]. The extensive development and use of hydrogen energy is conducive to the pursuit of carbon neutrality and emission peak. Hydrogen produced by the hydrolysis of sodium borohydride (NaBH₄) has been regarded as one of the most promising hydrogen production methods due to the advantages of high theoretical hydrogen production density (10.8 wt%), low hydrogen release temperature, controllable reaction process, high hydrogen purity, and environmental friendliness [4]. However, the slow hydrolysis reaction limits the wide use of hydrogen.

In order to accelerate the reaction kinetics of hydrolysis NaBH₄, a variety of catalysts such as Co [5–8], Ni [9–11], Rh [12], Pd [13], Ru [14,15], and Pt [16,17] have been comprehensively studied. Although Pt-based catalysts are one of the most active catalysts, the scarce storage and expensive price are the main obstacles to their large-scale application. Therefore, increasing the utilization efficiency of Pt remains the focus of the search. Previous studies have demonstrated that combining Pt with non-noble metals (such as Co [18,19],

Ni [20–22], and Fe [23,24]) could significantly improve the utilization efficiency of the catalysts. For example, Shumin Han et al. synthesized a carbon nanosphere (CNS)-supported ultrafine bimetallic Pt-Co nanoparticle (CNSs@Pt_{0.1}Co_{0.9}) catalyst for NaBH₄ catalysis. The as-prepared CNSs@Pt_{0.1}Co_{0.9} catalyst exhibited excellent performance in kinetic and thermodynamic tests [25]. Younghun Kim et al. designed a magnetic core and multi-shelled silica/titania-supported bimetallic (Pt/Ni NPs Fe₃O₄@SiO₂@TiO₂) catalyst for catalyzing the hydrolysis of NaBH₄ [20]. Jong-Sung Yu et al. uniformly deposited PtFe hydroxide by in situ hydrolysis of urea, followed by the preparation of a carbon-supported PtFe catalyst in ethylene glycol, and the catalyst exhibited excellent electrocatalytic performance [24].

Recently, Ni combined with precious metals, such as Pt-Ni and Ru-Ni, have been confirmed to be effective catalysts for hydrogen production from hydrolysis NaBH₄ [26–28]. However, these catalysts exhibit poor catalytic activity due to the accumulation of metal nanoparticles (NPs) during the reaction. Strategies including structural and morphology control, as well as the addition of suitable carriers can effectively inhibit the agglomeration problem [29–31]. In addition, the introduction of support material not only is conducive to the distribution of metal NPs but also improves the metal properties through geometric and electronic effects. Anelia Kakanakova-Georgieva et al., employing theoretical calculations, demonstrated that the porous structural material and the synergistic effect between metal NPs with support materials played an important role in the activity of the catalyst [32,33]. Porous hollow structures assembled from nanosheets with large surface areas could provide a unique microenvironment both on the inside and outside through species channels for guest shuttling [34]. Among numerous porous materials, metal-organic frameworks (MOFs) with tunable metal ions and organic ligands are extensively searched in the fields of energy storage and catalysis [35]. Furthermore, they also act as a self-sacrificing template in preparing the porous hollow materials. For example, pioneering studies used the Ti-MOFs as carriers to improve the catalytic performance of metal catalysts for hydrogen production [36,37]. Therefore, reasonably designed porous structural carriers for the dispersion of metal NPs enables the achievement of a satisfactory catalytic performance.

Herein, PtNi NPs were confined in a porous titanium oxide cage (PTOC) derived from NH₂-MIL-125 (Ti) by a facile hydrothermal method and used for the hydrogen production of hydrolysis NaBH₄. The synthesized catalysts exhibit good catalytic activity with a high hydrogen generation rate (10,164.3 mL·min⁻¹·g⁻¹) and low activation energy (28.7 kJ·mol⁻¹). In addition, the robust porous structure of PTOC benefits from the distribution of PtNi alloy particles and suppresses the agglomeration issue; thus, the PtNi/PTOC nanocomposite catalyst retains 87.8% of the initial catalytic activity after eight cycles.

2. Materials and Methods

2.1. Materials

All chemicals were of analytical grade and used without further purification. 2-aminoterephthalic acid, sodium borohydride (NaBH₄), and nickel nitrate hexahydrate (Ni(NO₃)₂·6H₂O) with a purity of 99% were purchased from Alfa Aesar Co., Ltd. (Tianjin, China). Chloroplatinic acid hexahydrate (H₂PtCl₆·6H₂O), titanium (IV) isopropoxide, L-alanine, and dimethylformamide (DMF) were purchased from Aladdin Reagent (Shanghai, China). All experiments were performed using DMF and anhydrous CH₃OH as solvents.

2.2. Synthesis of NH₂-MIL-125

The preparation of NH₂-MIL-125 nanocrystals followed a previously reported process [38]. Using DMF and ethanol as organic reaction solvents, 2-aminoterephthalic acid (500 mg, 2.76 mmol) was dissolved in a mixture solvent (10 mL) of 1 mL of CH₃OH (1 mL) and DMF (9 mL). Subsequently, 0.76 mmol of titanium isopropoxide was slowly added to the mixture under ultrasound. The solution was then placed in a 25 mL Teflon-lined reactor and heated at 150 °C for 72 h. After, the mixture was cooled to room temperature and the yellow powder was recovered by centrifugation. To remove impurities, the collected

powder was washed sequentially with DMF, ethanol, and deionized water and dried at 80 °C for 12 h.

2.3. Synthesis of PTOC

NH₂-MIL-125 (10 mg) was sonicated and dispersed in 5 mL of anhydrous ethanol. Next, 47.5 mg of L-alanine was added to the mixture and stirred for 6 h. The solution was then placed in a reaction vessel containing 25 mL of Teflon liner and heated at 176 °C for 36 h. The white precipitate was recovered by centrifugation, washed with ethanol, and dried under vacuum at 80 °C for 12 h.

2.4. Preparation of PtNi/PTOC

Amino acid molecules (generally a class of mild reducing agents) are used to prepare metal NPs. Herein, NH₂-MIL-125 (10 mg) was sonicated and dispersed in 5 mL of anhydrous ethanol. Then, L-alanine (47.5 mg) was added into the mixture and stirred for 6 h. H₂PtCl₆·6H₂O (1.0 mg, 2.3 μmol) and Ni(NO₃)₂·6H₂O (3 mg, 10.3 μmol) were added sequentially and stirred for 1 h. Then, the mixture was placed in a 25 mL Teflon pan and heated at 176 °C for 36 h. After centrifugation, the mixture was dried with ethanol at 80 °C for 12 h. For the comparison, Ni(NO₃)₂·6H₂O was not added in the preparation process of Pt/PTOC, and H₂PtCl₆·6H₂O was not added to Ni/PTOC; the other steps were consistent with the preparation process of PtNi/PTOC.

2.5. Characterization

The morphology of the PtNi/PTOC catalyst was analyzed by scanning electron microscopy (SEM, Quanta 200, FEI, Hillsboro, OR, USA) under a vacuum environment and 30 kV AC voltage. The test sample was dispersed on conductive material and stuck on a small sample holder. Excess powder was blown off with gas to avoid contaminating the cavity. The morphology and elemental composition of the catalyst was analyzed using a transmission electron microscope (TEM, JEOL 2010, JEOL, Tokyo, Japan) and dispersive X-ray detector (EDX) with an informal resolution of 0.12 nm and a point resolution of 0.25 nm. The powder was put into an anhydrous ethanol solution, shaken well with ultrasonic waves, and dropped onto the microgrid support film to obtain the sample to be tested. The chemical structure of the catalyst was characterized by Fourier-transform infrared (FT-IR) spectroscopy (Nicolet 6700, Waltham, MA, USA) in the wavenumber range of 400–4000 cm⁻¹. The fine powder of the sample was uniformly dispersed in potassium bromide in the ratio of 1:100 (m_{catalyst}:m_{KBr}) and the transparent flakes were obtained by the tablet method at the pressure of 5 MPa for 30 s. The crystal structure was analyzed by X-ray diffraction (XRD, 1820, Philips, Amsterdam, The Netherlands), with a scan angle from 5° to 90°, a step size set to 0.02, a working voltage of 40 kV, and a working current of 40 mA. The sample preparation was carried out as follows: the powder sample was evenly distributed in the sample holder and compacted with the glass plate. The sample surface was required to be smooth and flush with the glass surface. The nitrogen-desorption isotherms of the PtNi/PTOC catalysts were investigated using a Quantachrome Autosorb-iQ2 adsorber. The specific surface area of PtNi/PTOC catalyst was determined using a fully automated ratio meter and porosity analyzer. The samples were degassed in a glass tube at 150 °C for 10 h and then analyzed in liquid nitrogen. The pore size of a pore of the PtNi/PTOC catalyst was determined by the BJH method. X-ray photoelectron spectroscopy (XPS; Thermo Electron ESCALAB 250, Waltham, MA, USA), was mainly used qualitatively and semi-quantitatively through the analysis of catalysts, the valence state, species class, and surface content. The sample was pressed on aluminum foil, the excitation light source was Al Kα (hν = 1486.6 eV), and the final XPS was calibrated by C 1s (284.8 eV).

2.6. Hydrogen Production Testing

The catalytic hydrogen generation experiments were measured on a self-built hydrogen generation device [39]. The volume of hydrogen produced was determined by the

equivalent displacement of water. First, 0.1 g of catalyst was added in a 125 mL conical flask. Next, 10 mL of the solution containing 1.5 wt% NaBH₄ and 5 wt% NaOH was injected into the conical flask. The produced gas was collected in a container filled with water after flowing through a condenser and dryer to remove water vapor. The volume of produced H₂ was measured by the water displacement method. The water was displaced into a 1 L flask through a tube connected with a gas-gathering container and weighted by an electronic balance (UX2200H, Shimadzu Corporation, Kyoto, Japan). A computer connected to the electronic balance was used to record water quality automatically. The hydrogen released per gram of catalyst per unit time (HGR) was calculated through the display on the computer. After one hydrolysis test was completed, the catalyst was immediately washed and dried for 12 h. Subsequently, a fresh 10 mL of the 1.5 wt% NaBH₄ and 5 wt% NaOH solution was added to repeat the above measurements.

The hydrogen generation rate (HGR) was calculated according to the following equation:

$$HGR = \frac{V_{H_2O}(\text{mL})}{t(\text{min}) \times m(\text{g})}$$

where V_{H_2O} is the volume of drained water, m is the total mass of the catalyst, and t is the total reaction time in minutes [40].

3. Results and Discussion

3.1. Catalyst Characterization

In this paper, PtNi/PTOC was synthesized by a simple hydrothermal method and wet-reduction method. Figure 1 shows a schematic diagram of the preparation of PtNi/PTOC (PTOC). First, a round cake of NH₂-MIL-125 (Ti) was obtained using 2-aminoterephthalic acid as organic ligands and titanium (IV) isopropoxide as a metal precursor. Then, PTOC with a porous hollow structure was formed into an alcoholic thermal process at 176 °C under auxiliary amino acid molecules L-alanine. Lastly, PtNi precursors were reduced to Pt₃Ni NPs by the L-alanine. The formation of PTOC involved the Kirkendall effect of Ti ion dissolution and recrystallization. The Ti(IV) ions were firstly dissolved from NH₂-MIL-125(Ti) nanocrystals by coordination of Ti(IV) with amino acids (L-alanine), leading to the formation of sheet-like titanium oxide NPs on the NH₂-MIL-125(Ti) nanocrystals. With this continuous transformation, successive shells of titanium oxides were generated and transferred into the completed porous cages.

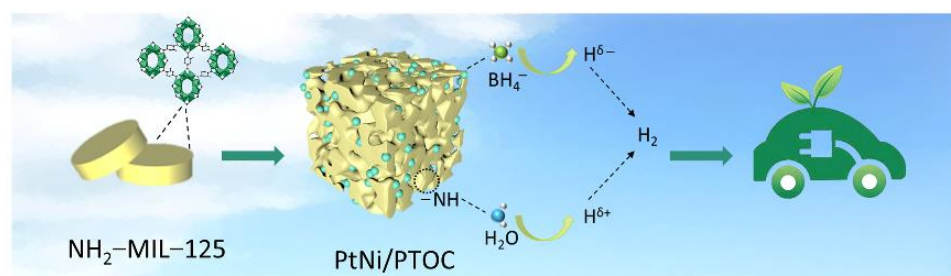


Figure 1. The illustration of the synthetic route of PtNi/PTOC.

The morphology of NH₂-MIL-125 and PTOC were characterized by SEM; as can be seen in Figure 2a,b, the NH₂-MIL-125 exhibits a round cake with a smooth surface, and the size is around 300–500 nm. After the auxiliary of the amino acid molecule L-alanine under hydrothermal circumstances, the cage structure of PTOC remains, with multi-channel interlacing on the surface (Figure 2c,d). Due to the alcoholization of NH₂-MIL-125, the nanosheets were assembled into a cage structure. L-alanine is commonly used as a mild reducing agent for the preparation of metal NPs [41,42]. After the hydrothermal reaction, PtNi precursors were reduced to Pt₃Ni NPs and confined in PTOC. As shown

in Figure 2e,f, compared with the PTOC sample, Pt-Ni/PTOC still retained the unique “nanocage” structure.

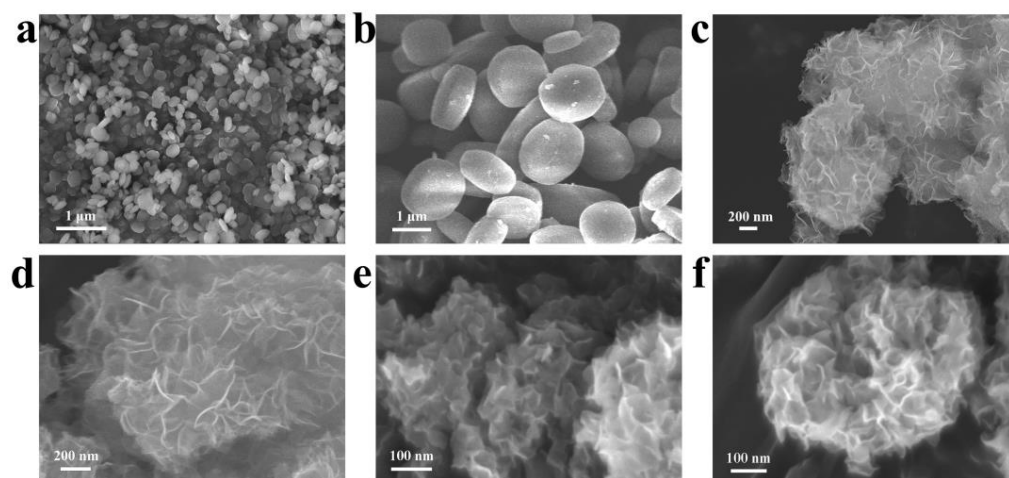


Figure 2. SEM images of (a,b) $\text{NH}_2\text{-MIL-125}$; (c,d) PTOC and (e,f) PtNi/PTOC catalyst.

As shown in Figure 3, HRTEM analysis showed that PtNi NPs were uniformly distributed in the PTOC nanocages with average particle sizes of 1.68 nm (Figure 3b). Further, high-resolution HRTEM analysis revealed that the d-spacing of 0.223 nm is between the (111) crystal faces of Pt (0.227 nm) and Ni (0.204 nm), indicating the formation of PtNi alloy NPs (Figure 3c) [43]. The HAADF-STEM image also confirmed the formation of uniformly distributed PtNi NPs (Figure 3d). EDX analysis showed that the as-prepared nanocomposites consisted of Ti, N, Pt, and Ni (Figure 3e–h). These results indicate that the 3D structure of PtNi NPs encapsulated by PTOC nanocages have been successfully prepared.

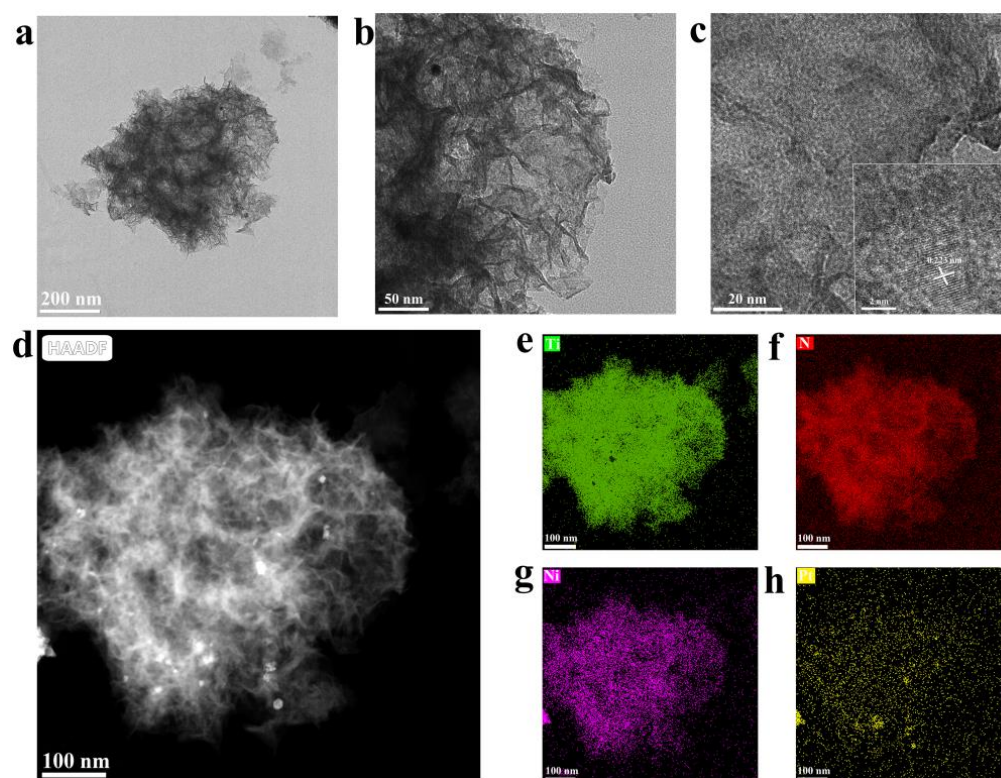


Figure 3. TEM images of (a,b) PtNi/PTOC catalyst; (c) HRTEM; (d) HAADF-STEM (e–h); EDX images of PtNi/PTOC.

FT-IR measurements (Figure 4a) were carried out to detect the functional groups of the as-prepared catalysts. The experimental results showed that all the prepared catalysts contained benzene rings and amino groups (the characteristic peaks at 3428 cm^{-1} and 1630 cm^{-1}). The existence of amino groups stably binds the metal NPs due to the strong chelation/complexation effect between the metal and amine groups [44]. Therefore, our results indicate that PTOC precursors are beneficial for the distribution of metal NPs. The XRD spectrum (Figure 4b) had four peaks at $2\theta = 25^\circ$, 48° , 55° , and 62° , which corresponded to the (101), (200), (211), and (213) crystal planes of anatase TiO_2 (PDF No. 21-1272). The diffraction peaks of layered titanate $\text{H}_2\text{Ti}_8\text{O}_{17}$ also appeared (PDF No. 36-0656), indicating that the PTOC had a two-component titanium oxide porous cage. In addition, the reflected signals of the Pt/PTOC and Ni/PTOC samples matched well with metallic Pt (PDF No. 87-0647) and Ni (PDF No. 65-0380), respectively. The diffraction peaks of PtNi alloy laid between the corresponding characteristic peaks of Pt and Ni, which further reflected the well-alloyed PtNi nanoparticles [45].

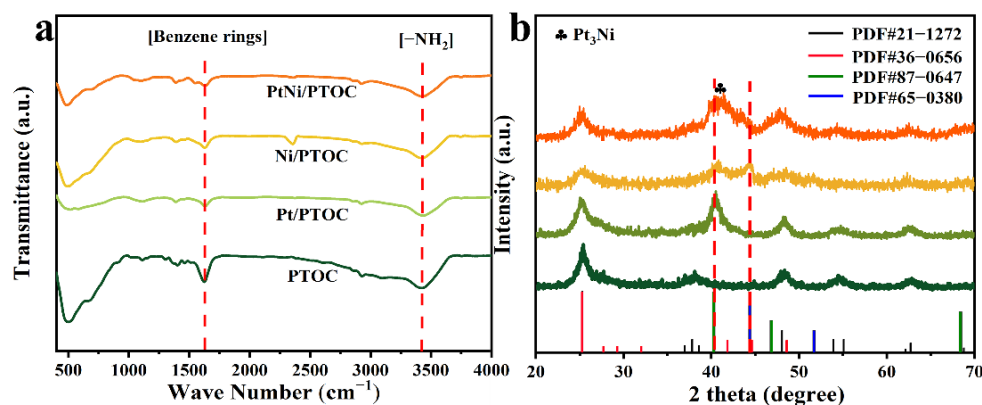


Figure 4. (a) FTIR spectra of catalysts. (b) XRD patterns of catalysts.

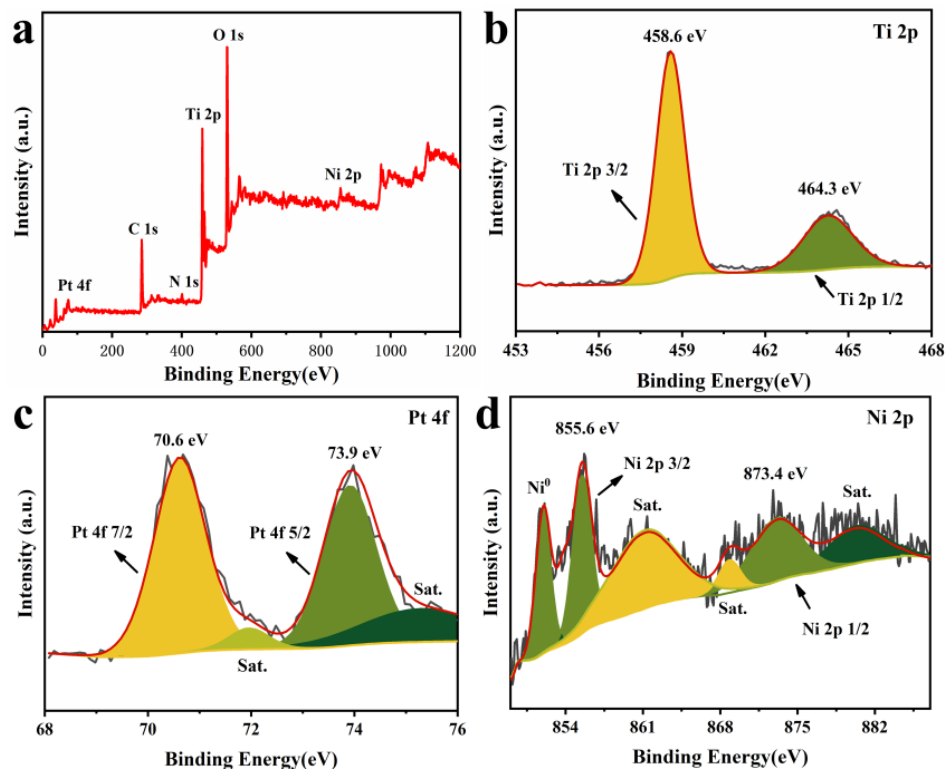


Figure 5. X-ray photoelectron spectra of Pt-Ni/PTOC catalyst (a) full spectrum; (b) Ti 2p; (c) Pt 4f; (d) Ni 2p.

The surface interactions and electronic state of PtNi/PTOC were investigated using XPS. Figure 5a shows the whole XPS pattern of PtNi/PTOC. The signals generated by the PTOC corresponded to C 1s, N 1s, O 1s, Ti 2p, Pt 4f, and Ni 2p. The narrow range spectra of Ti 2p is depicted in Figure 5b, which also proves the presence of PTOC. In Figure 5c, it can be seen that the Pt 4f region of core level binding energies is deconvoluted into two sets of spin-orbit doublet peaks. The Pt 4f spectrum exhibited two peaks at 71.4 and 74.7 eV and were assigned to Pt 4f7/2 and Pt 4f5/2, respectively, suggesting the presence of Pt⁰. Two peaks at 71.9 and 75.3 eV corresponded to the satellite peaks of Pt. The binding energy located at 855.6 and 873.4 eV belonged to the Ni 2p3/2, and Ni 2p1/2, respectively. The binding energies at 861.38, 868.92, and 873.4 eV corresponded to the satellite peaks. In addition, the binding energy around 852.05 eV is attributed to the Ni⁰ peak, which confirmed the existence of metallic Ni in PtNi/PTOC (Figure 5d). The strong interaction between Pt and Ni within the catalyst may lead to an increased oxidation resistance, which is beneficial to the catalysis activity and durability [46].

As shown in Figure 6a, PtNi/PTOC exhibited a typical IV-type isotherm with obvious hysteresis loops with a high specific surface area of approximately 206.2 m²·g⁻¹. In addition, PTOC showed that similar isotherms with the specific surface area decreased from 206.2 m²·g⁻¹ to 145.8 m²·g⁻¹, which is due to the addition of PtNi NPs. From the IV-type isotherms with obvious hysteresis loops, the main pore size distribution of two materials is mesopores. Pore-size distribution curves showed that the size of the pore in PtNi/PTOC ranged from 3.5 nm to 10.0 nm (Figure 6b). The rich mesopores are conducive to the penetration of the electrolyte and the transport of electrons, thereby enhancing the catalytic activity of the material.

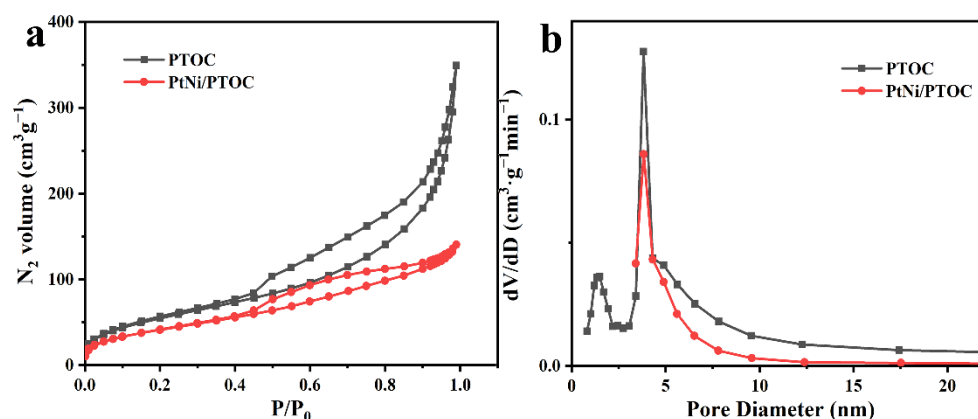


Figure 6. N₂ desorption/adsorption isotherm (a) and pore-size distributions (b) for PTOC and PtNi/PTOC.

3.2. Effect of Different Types of Catalysts

The effect of different catalysts on the hydrolysis of NaBH₄ under alkaline conditions was investigated. As shown in Figure 7, PtNi/PTOC exhibited optimal performance with hydrogen release rate (HGR) of 10,164.3 mL·min⁻¹ at 25 °C, which is higher than Pt/PTOC and Ni/PTOC. Compared to most of the previously reported results, PtNi/PTOC also exhibited a good catalytic activity (Table 1) [25,47–52]. According to Figure 7b, the magnitude of the catalytic performance was PtNi/PTOC > Pt/PTOC > Ni/PTOC, while PTOC and NH₂-MIL-125 had no catalytic activity. The experimental results show that the synergistic effect between Pt and Ni enhanced the catalytic activity more than the single Pt or Ni-based catalyst, thereby promoting the rapid release of hydrogen from NaBH₄. Furthermore, the evenly distributed PtNi alloy particles with more catalytically active sites simultaneously enhanced the hydrolysis activity.

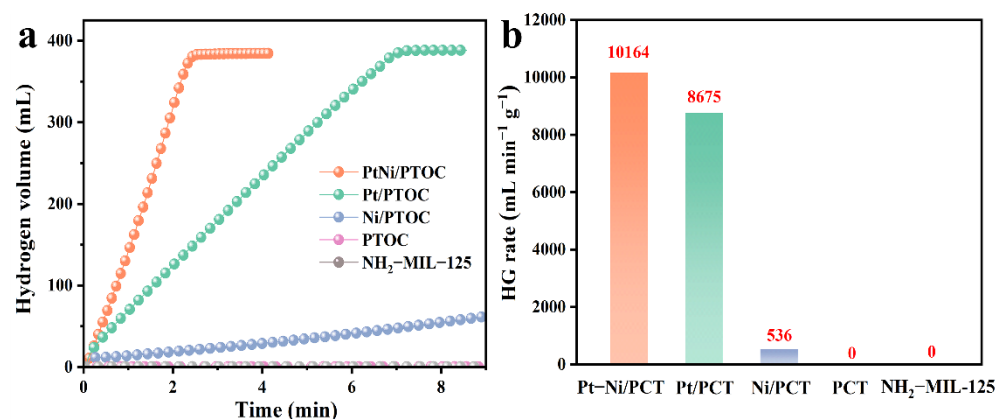


Figure 7. Hydrogen volume versus time (a) and HG rate bar chart of NH₂-MIL-125, PTOC, Pt/PTOC, Ni/PTOC, and (b) PtNi/PTOC (reaction conditions: batch system, 25 °C, 1.5 wt% NaBH₄ + 5 wt% NaOH, 0.1 g catalyst).

Table 1. Comparison of catalyst systems, reaction temperatures, HGR, E_a values, and number of cycles for NaBH₄ hydrolysis catalyzed by various catalysts.

Sample	Temperature (°C)	HG Rate (mL·min ⁻¹ ·g _M ⁻¹)	E_a (kJ·mol ⁻¹)	Number of Cycles	Cyclic Stability	Ref.
CNSs@Pt _{0.1} Co _{0.9}	30	8943.0	38.0	5	85.2%	[25]
Pt/MWCNTs	30	16.9	46.2	5	80.0%	[47]
Pt/CeO ₂ -Co ₇ Ni ₂ O _x	25	7834.8	47.4	5	85.0%	[48]
PtPd/GO	25	3940.0	29.4	4	60.0%	[49]
Pt/Si ₃ N ₄	80	13,000.0	35.2	5	82.5%	[50]
NiCoP NA/Ti	30	3016.8	52.7	8	70.0%	[51]
RuNi/Ti ₃ C ₂ ×2	30	1649.0	34.7	4	50%	[52]
PtNi/PTOC	29	10,164.3	28.7	8	87.8%	This work

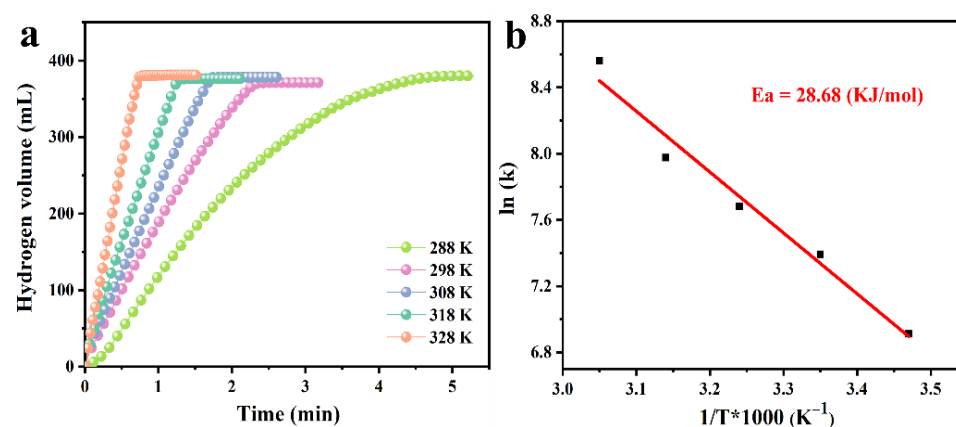


Figure 8. (a) Hydrogen generation kinetics curves and (b) Arrhenius plot obtained using 1.5 wt% NaBH₄ and 1.0 wt% NaOH solution and employing PtNi/PTOC as a catalyst at different solution temperatures.

In order to measure the activation energy (E_a) of the hydrolysis reaction, hydrolysis tests were carried out using different temperatures with the other parameters unchanged, controlling the reaction temperature from 15 to 55 °C (Figure 8a) with a gradient of 10 °C. As expected, all of the tests reached the theoretical hydrogen quantity, and the hydrogen release rate increased with the increase in reaction temperature, which belongs to the first-order reaction [53–55]. According to the Arrhenius slope calculation, the activation energy of Pt-Ni/PTOC is 28.7 kJ·mol⁻¹ (Figure 8b), which was lower than most of the catalysts that

have been reported (Table 1). The synergistic effect between PtNi NPs and PTOC may be the main factor for the decrease in the E_a value. The small particle size of the PtNi NPs is well supported on the pores of PTOC, thus avoiding excessive losses and agglomeration during hydrolysis. Moreover, the porous hollow structure promotes the interaction mass transfer between the catalyst and NaBH_4 in the pores. Therefore, these results show that PtNi/PTOC has good kinetic properties for catalyzing NaBH_4 hydrogen release.

3.3. Stability of PtNi/PTOC

The stability of the catalyst is a key index to the actual application of hydrogen generation from NaBH_4 hydrolysis. Figure 9 shows that the PtNi/PTOC catalyst was tested eight times under conventional conditions ($25\text{ }^\circ\text{C}$). The catalytic activity of the hydrogen evolution of NaBH_4 decreased slightly and maintained the initial catalytic activity of 87.8% after eight cycles. The excellent cycling performance may be related to the hollow porous structure of PTOC, not only providing a large surface area for the distribution of PtNi alloy particles but also suppressing the agglomeration issues.

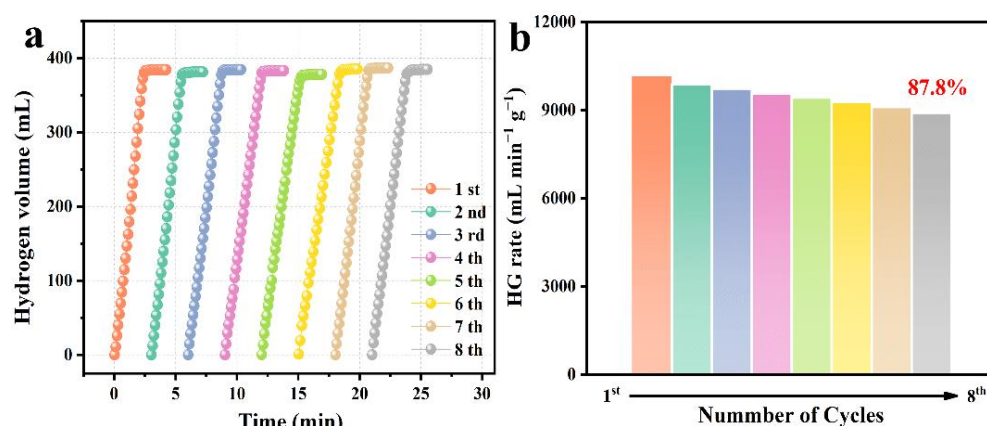


Figure 9. (a) Reusability of PtNi/PTOC with 0.1 g catalyst and 1.5 wt% NaBH_4 + 5 wt% NaOH solution at $25\text{ }^\circ\text{C}$; (b) HG rate bar chart of catalyst used 8 times.

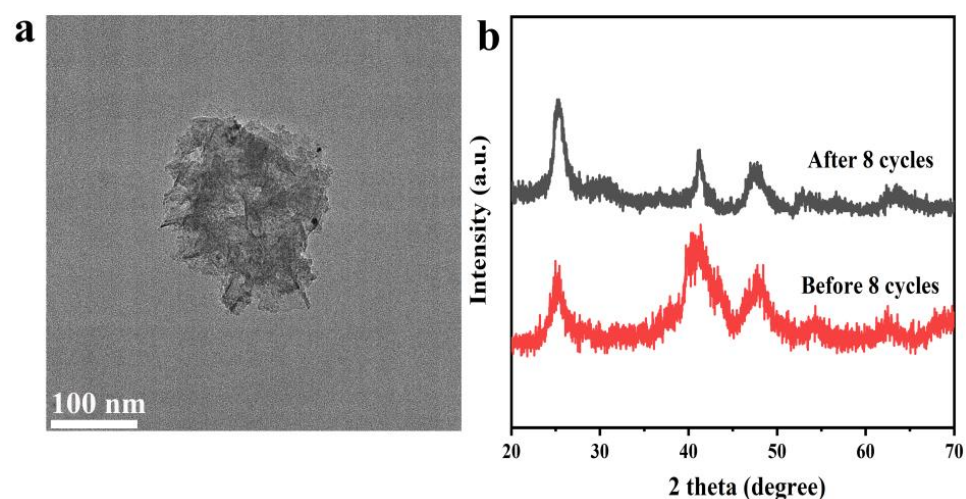


Figure 10. (a) TEM images of the PtNi/PTOC catalyst after 8 cycles; (b) XRD patterns of the PtNi/PTOC catalyst before cycling and after 8 cycles.

To verify the structural stability of the PtNi/PTOC catalyst, TEM (Figure 10a) and XRD characterizations were carried out after the cyclability test (Figure 10b). The TEM images of PtNi/PTOC after cycle tests show that the material maintained the nanocage structure with numerous sheets, indicating the stable structural integrity of the catalyst. In addition,

compared to the original PtNi/PTOC sample, there was no significant agglomeration, which is favorable for the catalytic reaction. The XRD spectra of the obtained products showed that two XRD spectra were well-matched, and the peak of the catalyst became sharp after cycle tests, indicating the increased crystallinity of the catalyst. According to the Scherrer formula, ($D = K\lambda / \beta \cos\theta$), the size of PtNi/PTOC catalyst increased from 1.68 to 2.32 nm after eight cycle tests, which was one of the reasons for the decay of catalytic activity. The stable structure and high catalytic activity of metal NPs are promising for the hydrolysis of borohydride.

4. Conclusions

In this work, ultra-small PtNi NPs were confined in a porous titanium oxide cage (PTOC) derived from NH₂-MIL-125 (Ti) by a facile hydrothermal method and used for the hydrogen production of hydrolysis NaBH₄. At a room temperature of 25 °C, the hydrogen production rate of PtNi/PTOC reached 10,164.3 mL·min⁻¹·g_M⁻¹, and the activation energy was 28.7 kJ·mol⁻¹. After eight cycles of testing, 87.8% of the initial test performance was maintained. Such excellent performance can be attributed to the following: (i) The porous and hollow structure of PTOC creates a unique microenvironment between its interior and exterior, which provides more reaction channels. (ii) PTOC with a high surface area enables the even distribution of PtNi alloy particles, thus exhibiting a large number of active sites. (iii) The synergistic effect between PTOC and PtNi alloy particles can improve the reactivity. (iv) The robust porous structure maintains the integrity of the catalyst and suppresses the aggregation of nanoparticles. The catalyst has the advantages of a simple operation and economic efficiency and shows promise for producing hydrogen for fuel-cell vehicles.

Author Contributions: Conceptualization, Y.Y. and L.K.; methodology, Y.Y. and L.K.; software, Y.Y., L.K., Z.S. and C.Z.; validation, Y.Y. and L.K.; formal analysis, C.Z., L.S. and F.X.; investigation, Y.Y., L.K., L.S. and F.X.; resources, L.S. and F.X.; data curation, Y.Y., L.K., Z.S. X.J., Q.S., Y.B., D.C., Y.X., K.Z. and B.L.; writing—original draft preparation, Y.Y., L.K. and C.Z.; writing—review and editing, L.S., F.X. and H.P.; visualization, Y.Y. and L.K.; supervision, L.S., F.X. and H.P.; project administration, L.S. and F.X.; funding acquisition, L.S. and F.X. All authors have read and agreed to the published version of the manuscript.

Funding: This work was supported by the National Key Research and Development Program of China (2018YFB1502103 and 2018YFB1502105), the National Natural Science Foundation of China (51971068, U20A20237 and 51871065), the Scientific Research and Technology Development Program of Guangxi (AA19182014, AD17195073 and AA17202030-1), Guangxi Bagui Scholar Foundation, Guangxi Collaborative Innovation Centre of Structure and Property for New Energy and Materials, Guangxi Advanced Functional Materials Foundation and Application Talents Small Highlands, Chinesisch-Deutsche Kooperationsgruppe (GZ1528), Science research and Technology Development project of Guilin (20210216-1) and Science Research and Technology Development Project of Guilin (20210102-4).

Institutional Review Board Statement: Not applicable.

Informed Consent Statement: Not applicable.

Data Availability Statement: Not applicable.

Conflicts of Interest: The authors declare no conflict of interest.

References

1. Chen, M.; Xiao, X.; Wang, X.; Lu, Y.; Zhang, M.; Zheng, J.; Chen, L. Self-templated carbon enhancing catalytic effect of ZrO₂ nanoparticles on the excellent dehydrogenation kinetics of MgH₂. *Carbon* **2020**, *166*, 46–55. [[CrossRef](#)]
2. Zhang, M.; Xiao, X.; Luo, B.; Liu, M.; Chen, M.; Chen, L. Superior de/hydrogenation performances of MgH₂ catalyzed by 3D flower-like TiO₂@C nanostructures. *J. Energy Chem.* **2020**, *46*, 191–198. [[CrossRef](#)]
3. Chen, W.; Xiao, X.; He, J.; Dong, Z.; Wang, X.; Chen, M.; Chen, L. A dandelion-like amorphous composite catalyst with outstanding performance for sodium borohydride hydrogen generation. *Int. J. Hydrogen Energy* **2021**, *46*, 10809–10818. [[CrossRef](#)]
4. Zhu, Y.; Ouyang, L.; Zhong, H.; Liu, J.; Wang, H.; Shao, H.; Huang, Z.; Zhu, M. Closing the Loop for Hydrogen Storage: Facile Regeneration of NaBH₄ from its Hydrolytic Product. *Angew. Chem. Int. Ed.* **2020**, *59*, 8623–8629. [[CrossRef](#)]

5. Huang, Y.; An, C.; Zhang, Q.; Zang, L.; Shao, H.; Liu, Y.; Yuan, H.; Wang, C.; Wang, Y. Cos-effective mechanochemical synthesis of highly dispersed supported transition metal catalysts for hydrogen storage. *Nano Energy* **2021**, *80*, 105535. [[CrossRef](#)]
6. Min, J.; Jeffery, A.; Kim, Y.; Jung, N. Electrochemical Analysis for Demonstrating CO Tolerance of Catalysts in Polymer Electrolyte Membrane Fuel Cells. *Nanomaterials* **2019**, *9*, 1425. [[CrossRef](#)] [[PubMed](#)]
7. Bu, Y.; Liu, J.; Chu, H.; Wei, S.; Yin, Q.; Kang, L.; Luo, X.; Sun, L.; Xu, F.; Huang, P.; et al. Catalytic Hydrogen Evolution of NaBH₄ Hydrolysis by Cobalt Nanoparticles Supported on Bagasse-Derived Porous Carbon. *Nanomaterials* **2021**, *11*, 3259. [[CrossRef](#)]
8. Ren, Y.; Wang, J.; Hu, W.; Wen, H.; Qiu, Y.; Tang, P.; Chen, M.; Wang, P. Hierarchical Nanostructured Co-Mo-B/CoMoO_{4-x} Amorphous Composite for the Alkaline Hydrogen Evolution Reaction. *ACS Appl. Mater. Interfaces* **2021**, *13*, 42605–42612. [[CrossRef](#)]
9. Shao, H.; Huang, G.; Liu, Y.; Guo, Y.; Wang, Y.N. Thermally stable Ni MOF catalyzed MgH₂ for hydrogen storage. *Int. J. Hydrogen Energy* **2021**, *46*, 37977–37985. [[CrossRef](#)]
10. Gao, H.; Shao, Y.; Shi, R.; Liu, Y.; Zhu, J.; Liu, J.; Zhu, Y.; Zhang, J.; Li, L.; Hu, X. Effect of Few-Layer Ti₃C₂T_x Supported Nano-Ni via Self-Assembly Reduction on Hydrogen Storage Performance of MgH₂. *ACS Appl. Mater. Interfaces* **2020**, *12*, 47684–47694. [[CrossRef](#)]
11. Liu, W.; Zhi, H.; Yu, X. Recent progress in phosphorus based anode materials for lithium/sodium ion batteries. *Energy Storage Mater.* **2019**, *16*, 290–322. [[CrossRef](#)]
12. Larichev, Y.V.; Netskina, O.V.; Komova, O.V.; Simagina, V.I. Comparative XPS study of Rh/Al₂O₃ and Rh/TiO₂ as catalysts for NaBH₄ hydrolysis. *Int. J. Hydrogen Energy* **2010**, *35*, 6501–6507. [[CrossRef](#)]
13. Liu, S.; Chen, X.; Wu, Z.J.; Zheng, X.C.; Peng, Z.K.; Liu, P. Chitosan-reduced graphene oxide hybrids encapsulated Pd (0) nanocatalysts for H₂ generation from ammonia borane. *Int. J. Hydrogen Energy* **2019**, *44*, 23610–23619. [[CrossRef](#)]
14. Konuş, N.; Karataş, Y.; Gulcan, M. In situ formed ruthenium (0) nanoparticles supported on TiO₂ catalyzed hydrogen generation from aqueous ammonia-borane solution at room temperature under air. *Synth. React. Inorg. Met. Org. Chem.* **2016**, *46*, 534–542. [[CrossRef](#)]
15. Zhang, J.; Lin, F.; Yang, L.; He, Z.; Huang, X.; Zhang, D.; Dong, H. Ultrasmall Ru nanoparticles supported on chitin nanofibers for hydrogen production from NaBH₄ hydrolysis. *Chin. Chem. Lett.* **2020**, *31*, 2019–2022. [[CrossRef](#)]
16. Dai, P.; Zhao, X.; Xu, D.; Wang, C.; Tao, X.; Liu, X.; Gao, J. Preparation, characterization, and properties of Pt/Al₂O₃/cordierite monolith catalyst for hydrogen generation from hydrolysis of sodium borohydride in a flow reactor. *Int. J. Hydrogen Energy* **2019**, *44*, 28463–28470. [[CrossRef](#)]
17. Ro, G.; Kim, Y. H₂ generation using Pt nanoparticles encapsulated in Fe₃O₄@SiO₂@TiO₂ multishell particles. *Colloids Surf. A* **2019**, *577*, 48–52. [[CrossRef](#)]
18. Chen, J.; Gu, Y.; Kong, D.; Xiang, S.; Wang, P.; Zhang, H.; Zhang, S. Preparation of Colloidal Pt/Co Bimetallic Nanoparticle Catalysts and Their Catalytic Activity for Hydrogen Generation from Hydrolysis Reaction of NaBH₄. *Rare Met. Mater. Eng.* **2014**, *43*, 2209–2214.
19. Kotkondawar, A.V.; Rayalu, S. Enhanced H₂ production from dehydrogenation of sodium borohydride over the ternary Co_{0.97}Pt_{0.03}/CeO_x nanocomposite grown on CGO catalytic support. *RSC Adv.* **2020**, *10*, 38184–38195. [[CrossRef](#)]
20. Ro, G.; Hwang, D.K.; Kim, Y. Hydrogen generation using Pt/Ni bimetallic nanoparticles supported on Fe₃O₄@SiO₂@TiO₂ multi-shell microspheres. *J. Ind. Eng. Chem.* **2019**, *79*, 364–369. [[CrossRef](#)]
21. Guo, H.; Chen, C.; Chen, K.; Cai, H.; Chang, X.; Liu, S.; Wang, C. High performance carbon-coated hollow Ni₁₂P₅ nanocrystals decorated on GNS as advanced anodes for lithium and sodium storage. *J. Mater. Chem. A* **2017**, *5*, 22316–22324. [[CrossRef](#)]
22. Aranishi, K.; Singh, A.K.; Xu, Q. Dendrimer-Encapsulated Bimetallic Pt-Ni Nanoparticles as Highly Efficient Catalysts for Hydrogen Generation from Chemical Hydrogen Storage Materials. *Chem. Cat. Chem.* **2013**, *5*, 2248–2252. [[CrossRef](#)]
23. Li, W.; Zhao, W.; Zhou, W.; Zhou, X.; Sun, L.; Zhang, H.; Lu, L.; Zhang, S. Fabrication and catalytic activity of Pt/Ni/Fe trimetallic nanoparticles for hydrogen generation from NaBH₄. *Chem. J. Chin. Univ. Chin.* **2014**, *35*, 2164–2169.
24. Yang, D.S.; Kim, M.S.; Song, M.Y.; Yu, J.S. Highly efficient supported PtFe cathode electrocatalysts prepared by homogeneous deposition for proton exchange membrane fuel cell. *Int. J. Hydrogen Energy* **2012**, *37*, 13681–13688. [[CrossRef](#)]
25. Zhang, H.; Zhang, L.; Rodríguez-Pérez, I.A.; Miao, W.; Chen, K.; Wang, W.; Han, S. Carbon nanospheres supported bimetallic Pt-Co as an efficient catalyst for NaBH₄ hydrolysis. *Appl. Surf. Sci.* **2021**, *540*, 14829. [[CrossRef](#)]
26. Qi, X.; Li, X.; Chen, B.; Lu, H.; Wang, L.; He, G. Highly active nanoreactors: Patchlike or thick Ni coating on Pt nanoparticles based on confined catalysis. *ACS Appl. Mater. Interfaces* **2016**, *8*, 1922–1928. [[CrossRef](#)] [[PubMed](#)]
27. Ghosh, S.K.; Mandal, M.; Kundu, S.; Nath, S.; Pal, T. Bimetallic Pt-Ni nanoparticles can catalyze reduction of aromatic nitro compounds by sodium borohydride in aqueous solution. *Appl. Catal. A Gen.* **2004**, *268*, 61–66. [[CrossRef](#)]
28. Hannauer, J.; Demirci, U.B.; Geantet, C.; Herrmann, J.M.; Miele, P. Transition metal-catalyzed dehydrogenation of hydrazine borane N₂H₄BH₃ via the hydrolysis of BH₃ and the decomposition of N₂H₄. *Int. J. Hydrogen Energy* **2012**, *37*, 10758–10767. [[CrossRef](#)]
29. Zhang, H.; Feng, X.; Cheng, L.; Hou, X.; Li, Y.; Han, S. Non-noble Co anchored on nanoporous graphene oxide, as an efficient and long-life catalyst for hydrogen generation from sodium borohydride. *Colloids Surf. A* **2019**, *563*, 112–119. [[CrossRef](#)]
30. Xia, G.; Zhang, L.; Fang, F.; Sun, D.; Guo, Z.; Liu, H.; Yu, X. General synthesis of transition metal oxide ultrafine nanoparticles embedded in hierarchically porous carbon nanofibers as advanced electrodes for lithium storage. *Adv. Funct. Mater.* **2016**, *26*, 6188–6196. [[CrossRef](#)]

31. Song, Q.; Wang, W.D.; Hu, X.; Dong, Z. Ru nanoclusters confined in porous organic cages for catalytic hydrolysis of ammonia borane and tandem hydrogenation reaction. *Nanoscale* **2019**, *11*, 21513–21521. [[CrossRef](#)] [[PubMed](#)]
32. Kakanakova-Georgieva, A.; Gueorguiev, G.; Sangiovanni, D.; Suwannaharn, N.; Ivanov, I.; Cora, I.; Pécz, B.; Nicotra, G.; Giannazzo, F. Nanoscale phenomena ruling deposition and intercalation of AlN at the graphene/SiC interface. *Nanoscale* **2020**, *12*, 19470–19476. [[CrossRef](#)] [[PubMed](#)]
33. Freitas, R.; Brito Mota, F.; Castilho, C.; Kakanakova-Georgieva, A.; Gueorguiev, G. Spin-orbit-induced gap modification in buckled honeycomb XBi and XBi₃ (X = B, Al, Ga, and In) sheets. *J. Phys.-Condens. Matter* **2015**, *27*, 485306. [[CrossRef](#)]
34. Chen, Y.; Shi, J. Chemistry of mesoporous organosilica in nanotechnology: Molecularly organic-inorganic hybridization into frameworks. *Adv. Mater.* **2016**, *28*, 3235–3272. [[CrossRef](#)] [[PubMed](#)]
35. Li, Y.; Xie, L.; Li, Y.; Zheng, J.; Li, X. Metal-Organic-Framework-Based Catalyst for Highly Efficient H₂ Generation from Aqueous NH₃BH₃ Solution. *Chem. Eur. J.* **2009**, *15*, 8951–8954. [[CrossRef](#)]
36. Yan, Y.; Li, C.; Wu, Y.; Gao, J.; Zhang, Q. From isolated Ti-oxo clusters to infinite Ti-oxo chains and sheets: Recent advances in photoactive Ti-based MOFs. *J. Mater. Chem. A* **2020**, *8*, 15245–15270. [[CrossRef](#)]
37. Karthik, P.; Shaheer, A.M.; Vinu, A.; Neppolian, B. Amine Functionalized Metal-Organic Framework Coordinated with Transition Metal Ions: D-d Transition Enhanced Optical Absorption and Role of Transition Metal Sites on Solar Light Driven H₂ Production. *Small* **2020**, *16*, 1902990. [[CrossRef](#)] [[PubMed](#)]
38. Gu, Z.; Chen, L.; Wang, H.; Guo, Y.; Xu, M.; Zhang, Y.; Duan, C. Light control of charge transfer in metal/semiconductor heterostructures for efficient hydrogen evolution: Optical transition versus SPR. *Int. J. Hydrogen Energy* **2017**, *42*, 26713–26722. [[CrossRef](#)]
39. Xu, F.; Zhang, X.; Sun, L.; Yu, F.; Li, P.; Chen, J.; Wu, Y.; Cao, L.; Xu, C.; Yang, X.; et al. Hydrogen generation of a novel Al-NaMgH₃ composite reaction with water. *Int. J. Hydrogen Energy* **2017**, *42*, 30535–30542. [[CrossRef](#)]
40. Yang, F.; Zou, Y.; Xiang, C.; Xu, F.; Sun, L. Synthesis of “needle-cluster” NiCo₂O₄ carbon nanofibers and loading of Co-B nanoparticles for hydrogen production through the hydrolysis of NaBH₄. *J. Alloys Compd.* **2022**, *911*, 165069. [[CrossRef](#)]
41. Zhou, H.; Kang, M.; Xie, B.; Wen, P.; Zhao, N. L-Alanine mediated controllable synthesis: Ultrathin Co₃O₄ nanosheets@ Ni foam for high performance supercapacitors. *J. Alloys Compd.* **2021**, *874*, 160030. [[CrossRef](#)]
42. Shen, Y.; Zhu, C.; Chen, B.; Chen, J.; Fang, Q.; Wang, J. Novel photocatalytic performance of nanocage-like MIL-125-NH₂ induced by adsorption of phenolic pollutants. *Environ. Sci. Nano* **2020**, *7*, 1525–1538. [[CrossRef](#)]
43. Wang, W.; Hong, X.; Yao, Q.; Lu, Z.H. Bimetallic Ni-Pt nanoparticles immobilized on mesoporous N-doped carbon as a highly efficient catalyst for complete hydrogen evolution from hydrazine borane. *J. Mater. Chem. A* **2020**, *8*, 13694–13701. [[CrossRef](#)]
44. Georgieva, J.; Valova, E.; Mintsouli, I.; Sotiropoulos, S.; Tatchev, D.; Armanyanov, S.; Malet, L. Pt (Ni) electrocatalysts for methanol oxidation prepared by galvanic replacement on TiO₂ and TiO₂-C powder supports. *J. Electroanal. Chem.* **2015**, *754*, 65–74. [[CrossRef](#)]
45. Liu, Y.; Chen, H.; Tian, C.; Geng, D.; Wang, D.; Bai, S. One-Pot Synthesis of Highly Efficient Carbon-Supported Polyhedral Pt₃Ni Alloy Nanoparticles for Oxygen Reduction Reaction. *Electrocatalysis* **2019**, *10*, 613–620. [[CrossRef](#)]
46. Li, M.; Zhu, Y.; Song, N.; Wang, C.; Lu, X. Fabrication of Pt nanoparticles on nitrogen-doped carbon/Ni nanofibers for improved hydrogen evolution activity. *J. Colloid Interface Sci.* **2018**, *514*, 199–207. [[CrossRef](#)]
47. Huff, C.; Quach, Q.; Long, J.M.; Abdel-Fattah, T.M. Nanocomposite catalyst derived from ultrafine platinum nanoparticles and carbon nanotubes for hydrogen generation. *ECS. J. Solid State Technol.* **2020**, *9*, 101008. [[CrossRef](#)]
48. Wu, C.; Zhang, J.; Guo, J.; Sun, L.; Ming, J.; Dong, H.; Yang, X. Ceria-induced strategy to tailor Pt atomic clusters on cobalt-nickel oxide and the synergetic effect for superior hydrogen generation. *ACS. Sustain. Chem. Eng.* **2018**, *6*, 7451–7457. [[CrossRef](#)]
49. Lu, L.; Shu, H.; Ruan, Z.; Ni, J.; Zhang, H. Preparation of Graphene-supported Pt-Pd Catalyst and Its Catalytic Activity and Mechanism for Hydrogen Generation Reaction. *Chem. J. Chin. Univ. Chi.* **2018**, *39*, 949–955.
50. Lale, A.; Wasan, A.; Kumar, R.; Miele, P.; Demirci, U.B.; Bernard, S. Organosilicon polymer-derived mesoporous 3D silicon carbide, carbonitride and nitride structures as platinum supports for hydrogen generation by hydrolysis of sodium borohydride. *Int. J. Hydrogen Energy* **2016**, *41*, 15477–15488. [[CrossRef](#)]
51. Li, K.; Ma, M.; Xie, L.; Yao, Y.; Kong, R.; Du, G.; Sun, X. Monolithically integrated NiCoP nanosheet array on Ti mesh: An efficient and reusable catalyst in NaBH₄ alkaline media toward on-demand hydrogen generation. *Int. J. Hydrogen Energy* **2017**, *42*, 19028–19034. [[CrossRef](#)]
52. Li, X.; Zeng, C.; Fan, G. Ultrafast hydrogen generation from the hydrolysis of ammonia borane catalyzed by highly efficient bimetallic RuNi nanoparticles stabilized on Ti₃C₂X₂ (X = OH and/or F). *Int. J. Hydrogen Energy* **2015**, *40*, 3883–3891. [[CrossRef](#)]
53. Pornea, A.M.; Abebe, M.W.; Kim, H. Ternary NiCoP urchin like 3D nanostructure supported on nickel foam as a catalyst for hydrogen generation of alkaline NaBH₄. *Chem. Phys.* **2019**, *516*, 152–159. [[CrossRef](#)]
54. Wang, Y.; Li, G.; Wu, S.; Wei, Y.; Meng, W.; Xie, Y.; Zhang, X. Hydrogen generation from alkaline NaBH₄ solution using nanostructured Co-Ni-P catalysts. *Int. J. Hydrogen Energy* **2017**, *42*, 16529–16537. [[CrossRef](#)]
55. Zhou, Y.; Fang, C.; Fang, Y.; Zhu, F.; Liu, H.; Ge, H. Hydrogen generation mechanism of BH₄⁻ spontaneous hydrolysis: A sight from ab initio calculation. *Int. J. Hydrogen Energy* **2016**, *41*, 22668–22676. [[CrossRef](#)]